Title

Interseismic megathrust coupling beneath the Nicoya Peninsula, Costa Rica, from the joint inversion of InSAR and GPS data

Journal

Journal of Geophysical Research: Solid Earth, 120(5)

ISSN

2169-9313

Authors

Xue, Lian
Schwartz, Susan
Liu, Zhen
et al.

Publication Date

2015-05-01

DOI

10.1002/2014jb011844

Peer reviewed

AGU PUBLICATIONS

JGR

Journal of Geophysical Research: Solid Earth

RESEARCH ARTICLE
10.1002/2014JB011844

Key Points:
- The interseismic strongly locked regions are the loci of coseismic slip
- InSAR integrated with GPS can recover deformation signals in subduction zones
- Our integrated model reveals more refined features than the GPS-only model

Supporting Information:
- Text S1–S7 and Figures S1–S8

Correspondence to:
L. Xue,
lxue3@ucsc.edu

Citation:
Xue, L., S. Schwartz, Z. Liu, and L. Feng (2015), Interseismic megathrust coupling beneath the Nicoya Peninsula, Costa Rica, from the joint inversion of InSAR and GPS data, *J. Geophys. Res. Solid Earth*, *120*, doi:10.1002/2014JB011844.

Received 25 DEC 2014
Accepted 7 APR 2015
Accepted article online 11 APR 2015

Interseismic megathrust coupling beneath the Nicoya Peninsula, Costa Rica, from the joint inversion of InSAR and GPS data

Lian Xue[1], Susan Schwartz[1], Zhen Liu[2], and Lujia Feng[3]

[1]Department of Earth and Planetary Sciences, University of California, Santa Cruz, California, USA, [2]Jet Propulsion Laboratory, California Institute of Technology, Pasadena, California, USA, [3]Earth Observatory of Singapore, Nanyang Technological University, Singapore, Singapore

Abstract The Nicoya Peninsula, Costa Rica, was struck by a long-anticipated and gap-filling M_w 7.6 earthquake in 2012. To study interseismic strain accumulation on the megathrust beneath the Nicoya Peninsula, we present an improved interseismic coupling model by integrating interferometric synthetic aperture radar (InSAR) and GPS data. Our model reveals three strongly coupled patches. The first strongly coupled patch locates beneath the Nicoya Peninsula and ruptured during the 2012 earthquake. The second strongly coupled patch locates offshore the central Nicoya Peninsula and remained largely unbroken. However, this region is close to and possibly intermingled with shallow slow slip and tremor, suggesting that accumulated strain in this region may be released both seismically and aseismically. The third strongly coupled patch offshore of the southeastern end of Nicoya overlaps part of the coseismic rupture of the 1990 M_w 7.0 Nicoya Gulf earthquake, indicating that significant strain has re-accumulated since this event. Incorporating InSAR data provides a more refined interseismic coupling model than using GPS alone and allows for a more reliable comparison with local seismic and aseismic activities. This comparison indicates that strongly locked regions during the interseismic stage are the loci of coseismic slip, and deep slow slip and low-frequency earthquakes occur in regions of low coupling or transition zones from low to high coupling, while shallow slow slip and tremor commingle with strongly coupled regions. Our study demonstrates that InSAR data can be used to recover small long-wavelength deformation signals with refined resolution in challenging subduction zone environments when integrated with GPS observations.

1. Introduction

Subduction zones generate the Earth's largest and most destructive earthquakes. The mechanical properties of the plate interface at subduction zones can be highly heterogeneous. Regions that accumulate strain during the interseismic period have been shown to be the loci of large coseismic slip [e.g., *Loveless and Meade*, 2011; *Metois et al.*, 2012; *Yue et al.*, 2013; *Zweck et al.*, 2002], while adjacent areas often host microearthquakes, slow slip, or seismic tremor [*Schwartz and Rokosky*, 2007]. In order to image the heterogeneity of the subduction zone interface and assess potential future seismic hazards, interseismic coupling on the plate interface must be determined.

For more than two decades, the Global Positioning System (GPS) has been a primary tool used to measure interseismic deformation and interrogate the degree of locking on the plate interface at subduction zones [e.g., *Dixon*, 1993; *Hyndman et al.*, 1995; *Mazzotti et al.*, 2000]. In general, GPS data provide excellent temporal resolution but have poor spatial coverage. In contrast, interferometric synthetic aperture radar (InSAR) data can alleviate these inadequacies, thus providing an excellent complement in spatial resolution to GPS observations but with coarse temporal sampling (e.g., days to weeks). Recently, InSAR has been widely used to measure coseismic deformation at subduction zones [e.g., *Biggs et al.*, 2009; *Pritchard and Fielding*, 2008; *Pritchard et al.*, 2002; *Tong et al.*, 2010]; however, using InSAR to measure subtle, long-wavelength signals, such as interseismic deformation, remains a challenge. The primarily offshore location of strain accumulation and concomitant low-amplitude interseismic deformation on land has impeded the success of InSAR in subduction zone environments. Therefore, most interseismic deformation studies using InSAR have been focused on continental fault zones [e.g., *Biggs et al.*, 2007; *Cavalié et al.*, 2008; *Fialko*, 2006; *Gourmelen et al.*, 2010]. Very few InSAR interseismic studies have been

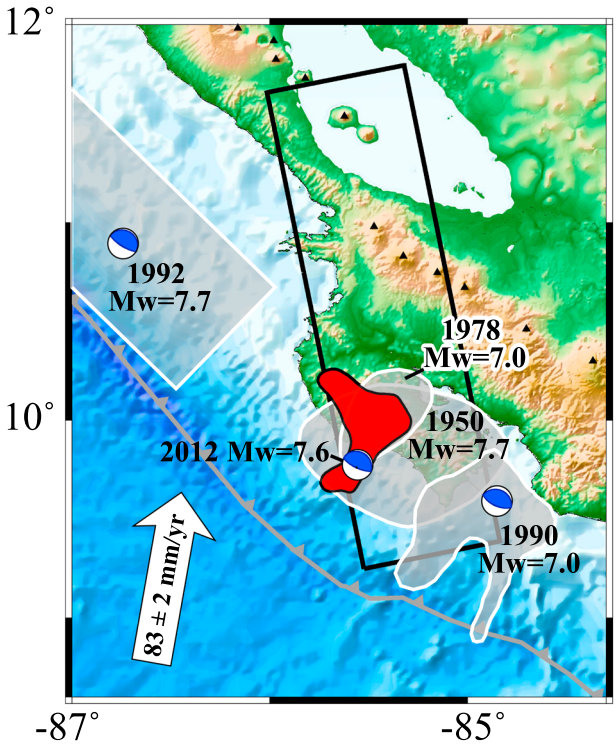

Figure 1. The tectonic setting of the Nicoya Peninsula. Aftershock areas of the 1950, 1978, 1990, and 1992 events are indicated with gray-filled patches. The coseismic region of the 2012 event is shown as the red-filled patch [*Yue et al.*, 2013]. Focal mechanisms for the 1990, 1992, and 2012 events from the global centroid moment tensor catalog are also indicated. The black rectangle indicates ALOS PALSAR track 164 used in this study. The white arrow indicates the convergence vector between the Cocos and Caribbean Plates [*DeMets et al.*, 2010]. The trench is marked with the gray barbed solid line. The black triangles are the Holocene active volcanoes [*Siebert and Simkin*, 2002].

published for subduction zones [*Bejar-Pizarro et al.*, 2013; *Cavalié et al.*, 2013; *Hooper et al.*, 2012]. The Nicoya Peninsula in Costa Rica lies directly above the seismogenic zone, which greatly improves its vantage point. The acquisitions of high quality L-band SAR observations over the Nicoya Peninsula between 2007 and 2011 enable us to construct an improved interseismic deformation map constrained by both InSAR and GPS data.

The Nicoya Peninsula is located directly above the subduction zone interface where the Cocos and Caribbean Plates converge at a rate of approximately 8 cm/yr [*DeMets et al.*, 2010] (Figure 1). The peninsula's unique location and the presence of a dense operating GPS and seismic network [*Outerbridge et al.*, 2010; *Walter et al.*, 2011] have made it a prime region to study strain accumulation and release at a subduction zone. During the last 160 years, four large megathrust earthquakes occurred beneath the Nicoya Peninsula in 1853, 1900, 1950 (M_w 7.7), and 2012 (M_w 7.6) [*Protti et al.*, 2014]. Moreover, since 2003, GPS and seismic networks on the Nicoya Peninsula have recorded seven slow-slip events (SSEs) accompanied by tremor [*Dixon et al.*, 2014; *Jiang et al.*, 2012; *Outerbridge et al.*, 2010; *Walter et al.*, 2011]. The most recent 2012 M_w 7.6 Nicoya earthquake ruptured a significant portion of a large locked patch previously identified using GPS data alone [*Feng et al.*, 2012], leaving another identified locked region offshore of the northwestern Peninsula unbroken [*Protti et al.*, 2014]. Understanding the detailed spatial distribution of the locked and creeping patches to assess whether the fully locked patches are distinct from and/or surrounded by slowly slipping regions is particularly important for earthquake hazard studies [*Schwartz and Rokosky*, 2007]. To better determine the location and size of locked patches and compare them to the ruptured and slow-slipping regions, this paper provides an improved interseismic coupling model by integrating InSAR and GPS data.

2. InSAR Data and Analysis

We use the L-band SAR data from the Advanced Land Observing Satellite (ALOS) Phase Array L-band Synthetic Aperture Radar (PALSAR) with ~23.6 cm wavelength. The dense vegetation on the Nicoya Peninsula limits the use of SAR data with shorter wavelengths because of low coherence of available interferograms. The SAR images were collected from January 2007 to October 2010 and are now archived at the Alaska Satellite Facility. Unfortunately, the ALOS PALSAR ceased operation in March 2011. Three ascending and three descending tracks are available for this region. However, the descending tracks have too few scene acquisitions, and the two adjacent ascending tracks have poor spatial coverage over our region of interest. Therefore, in our analysis, we only use ascending track 164 that provides enough SAR acquisitions and covers nearly the entire area of the Nicoya Peninsula (Figure 1) to image its interseismic deformation.

2.1. InSAR Data Processing

We processed 18 SAR acquisitions from track 164 between 2007 and 2010 by using the Jet Propulsion Laboratory/California Institute of Technology Repeat Orbit Interferometry Package [*Rosen et al.*, 2004] version 3.0.1. We constructed 120 possible interferograms with perpendicular baselines less than 1200 m. We used a Shuttle Radar Topography Mission version 3 digital elevation model, which has a 90 m resolution (downloaded from http://dds.cr.usgs.gov/srtm/version2_1/SRTM3/South_America/) to remove the topographic phase from the interferograms. Decorrelation of the interferograms is significant due to the heavy vegetation of the Nicoya Peninsula, so we reduced (complex averaged) the interferograms in the range and azimuth direction by 16 and 32 pixels to improve the signal coherence, resulting in a pixel size of ~75 m × 113 m in radar coordinate. We used the SNAPHU program [*Chen and Zebker*, 2000] to unwrap the phase. We used a triplet stacking phase which forms a loop as an indicator for the unwrapping errors [*Biggs et al.*, 2007]. Very localized unwrapping errors might still remain in the interferograms, but these are typically small and do not introduce major errors into the analysis of the interferograms.

2.2. Orbital Error Correction

One of the main issues in InSAR analysis is proper removal of residual orbital errors. These errors contribute to phase artifacts in the interferograms because of uncertainty in orbital parameters. Typical orbital errors are on the order of ~0.19 mm/km over space [*Fattahi and Amelung*, 2014; *Hanssen*, 2001]. To avoid tectonic signals being masked by long-wavelength orbital signals, a correction for the residual orbital signals is necessary. However, because of the spatially long-wavelength nature of interseismic deformation [e.g., *Bürgmann et al.*, 2000; *Simons and Rosen*, 2007], it is difficult to identify a subregion that is completely free of the deformation signal in order to estimate and correct for orbital errors. Moreover, the distribution of GPS stations is sparse in the northern region of the Nicoya Peninsula, so accurate corrections cannot be made using these GPS stations alone. Therefore, we corrected for residual orbital signals using a GPS-derived interseismic strain accumulation model from *Feng et al.* [2012]. The long-wavelength deformation information in the corrected InSAR data is maintained and should be similar to the GPS data. Since this GPS-derived interseismic model includes all of the GPS stations and fits the observations very well, it provides reliable information on the long-wavelength deformation.

First, we projected the predicted horizontal and vertical components of the GPS-derived interseismic velocities to the line of sight (LOS) direction by using a unit vector of LOS [0.60,0.13,0.79] in the east, north, and vertical directions. Then we removed the predicted LOS deformation from the unwrapped interferograms and applied a polynomial fit to remove the residual orbital error. Finally, we added the predicted LOS deformation back to the signals. This correction is similar to the SURF approach of *Tong et al.* [2013]. We do not observe significant stratified atmospheric noise in the remaining phase signal, so no correction for stratified atmospheric noise is included. We chose a point outside of the deformation region as a reference (Figure 3) and subtracted the mean value of the pixels around the reference point from all pixels in the images. This reference point also collocates with a campaign GPS station (BAGA) with a LOS velocity of ~9 mm/yr, which is relatively small compared with the other stations in the fore-arc region.

2.3. Stacking

In order to access whether InSAR can detect the interseismic deformation signal, we constructed a simple rate map by stacking. We selected eight corrected SAR interferograms, whose perpendicular baseline is $<$300 m and temporal duration is $>$2 year, to construct a time-weighted stacked image. Repetitions of the selected master or slave SAR acquisitions (Figure 2) are limited to no more than four. Assuming the interseismic deformation accumulates at a constant rate, the stacked velocity for each pixel can be expressed as $d_a = \sum_i^n d_i \Big/ \sum_i^n T_i$, where d_a is the average displacement over one year, d_i is the ith displacement during time T_i, and n is the number of selected pairs. The interferograms with longer time intervals contribute more to the stacking result. Stacking is based on pixels, and the number of interferograms used for stacking can be different for each pixel. The resultant LOS rate map shows two significant regions of deformation in the southern part of the peninsula with magnitudes of ~10–15 mm/yr, comparable to the GPS observations. It also shows deformation features that are correlated with the

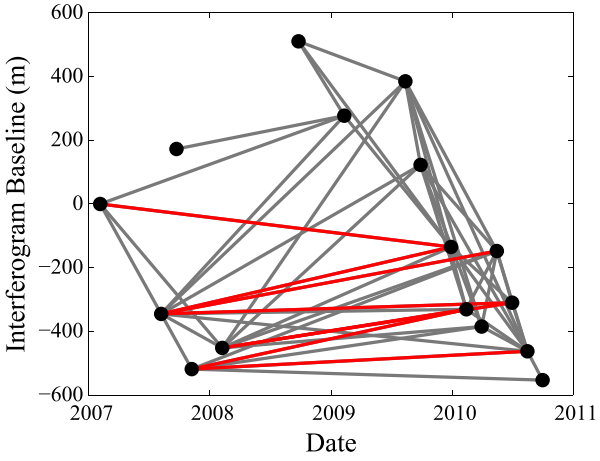

Figure 2. Time interval and spatial baseline of the 52 interferograms. The red lines indicate the interferograms selected for stacking.

location of volcanoes that are not obvious in the GPS measurements. In general, the stacked rate map is noisier near the coastal region and northern portion of the image than the rest of the area (Figure 3).

2.4. Time Series

To make use of all available SAR data, we used the small baseline subset method to invert for the LOS displacement time series from January 2007 to October 2010 at each pixel [*Berardino et al.*, 2002]. First, we used all possible interferograms to construct a time series and calculate the root-mean-square (RMS) difference between the observed interferograms and the reconstructed interferograms from the inverted time series for all the interferograms [*López-Quiroz et al.*, 2009]. We then chose 54 interferograms with the smallest RMS (Figure 2) to invert for the final time series. We applied a Gaussian function with a half width of 0.25 year as a temporal smoothing filter to the final time series to suppress atmospheric noise [e.g., *Berardino et al.*, 2002; *Liu et al.*, 2011]. The final time series still have considerable scatter due to residual atmospheric noise. Examination of individual time series shows no clear signals related to known SSEs that occurred in 2007 and 2009 during the InSAR data period [*Jiang et al.*, 2012]. Since we are focused on average "interseismic" strain accumulation (see discussion in section 5.1), we estimated a constant linear velocity by using linear regression of the time series for each coherent pixel. Scattering in the InSAR residual LOS time series after linear fitting is ~5.4 mm, and the typical total displacement of the slow-slip events in the LOS direction is ~6.4 mm. This suggests that using InSAR time series to detect transient slow-slip events in this region will be challenging. The major features of the linear rate map are similar to the stacking result (Figure 4), but the linear rate map shows a much cleaner pattern (Figure 3). Our ultimate goal is to combine the linear rate map from the InSAR time series analysis and GPS velocities to construct an interseismic coupling model.

Since the InSAR image has tens of thousands of data points, we applied a quadtree algorithm based on variance change to downsample the InSAR linear rate map [*Jónsson et al.*, 2002]. For the variance threshold of 0.81 cm^2, the downsampled linear rate map approximates the original LOS displacement well (see the supporting information). Since the signal in the vicinity of the volcanic arc is not related to the interseismic deformation, we masked the signal in this region. After downsampling the total number of pixels is 988.

2.5. Error Analysis

To assess uncertainties of model parameters, it is useful to characterize the noise level in the data. One of the main sources of spatially correlated noise in InSAR data comes from residual atmospheric signal [e.g., *Hanssen*, 2001; *Lohman and Simons*, 2005; *Liu et al.*, 2014]. To estimate the contribution of this spatially correlated noise in the linear rate map, we adopted a sample covariogram approach, in which the atmospheric errors can be approximated as spatially stationary and isotropic. The definition of the sample covariogram is

$$\hat{C}(h) = \frac{1}{2N}\sum_{i-l}^{n} d(r_i)\cdot d(s_i);$$

where N is the number of pixel pairs at location r_i and s_i, which satisfy $||r_i - s_i|| = h$; h is the distance between pixel pairs; and $d(r_i)$ is the observation at pixel r_i [*Hanssen*, 2001; *Lohman and Simons*, 2005]. We masked the signal at the southern end of the peninsula and near the volcanic arc to assure that no deformation signal is included in the atmospheric noise estimation (Figure 5a). The sample covariogram is calculated by averaging the covariance of each pixel pair within 100 m intervals in the distance range from 0 to 50 km. We used an

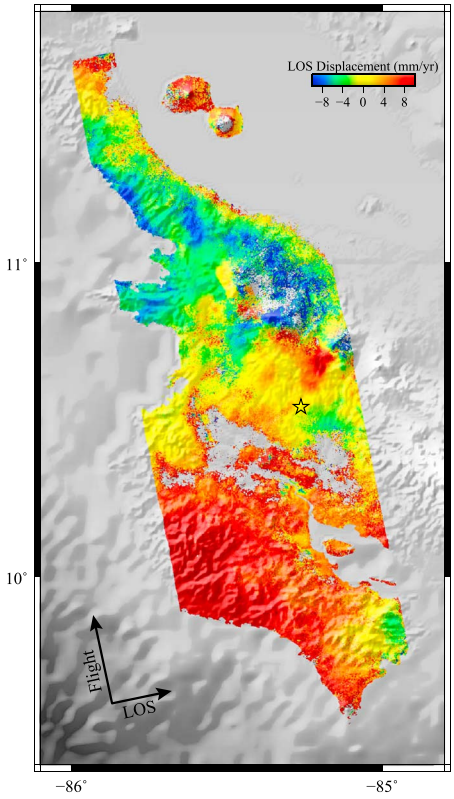

Figure 3. Average velocity map constructed by stacking the eight interferograms with durations longer than 2 years and baselines under 300 m. The arrow shows the line of sight and flight directions. Positive displacements indicate surface motion away from the satellite. The black star indicates the reference point.

empirical covariance function $\hat{C}(h) = \sigma^2 e^{-x/L}$ [*Hanssen*, 2001] to fit the calculated sample covariogram. For the linear rate map, the estimated σ^2 is 6.5 mm^2 and L is 35.2 km (Figure 5b). To construct the covariance matrix of the quadtree sampled linear rate map, we propagated the covariance of each pair, which was calculated by the estimated covariance function, into the corresponding quadtree square [*Sudhaus and Sigurjón*, 2009]. This covariance matrix was used in the InSAR/GPS joint inversion for interseismic coupling.

In order to assess the effects of this spatially correlated noise in the inversion, we generated a synthetic atmospheric signal (Figure 5c) by using the estimated covariance matrix of the quadtree sampled linear rate map [*Parsons et al.*, 2006]. The simulated synthetic atmospheric noise has similar characteristics to the noise in the linear rate map, so it presents a good approximation for the residual atmospheric noise in the data. This synthetic atmospheric signal was used in the checkerboard test to include the influence of the spatial correlated noise.

3. GPS Data

The continuous and campaign GPS interseismic velocities used in our model are taken from *Feng et al.* [2012]. There are 19 continuous GPS stations (installation initiated in 2002 and completed in late 2009 [*Outerbridge et al.*, 2010]) and 29 campaign stations (which were occupied at least twice for three consecutive days each time) [*Feng et al.*, 2012]. These GPS data have different observation periods, but most of them overlap the temporal coverage of the InSAR data. The GPS network covers the entire Nicoya Peninsula (Figure 6a). To better constrain the downdip limit of the seismogenic zone, we included high-quality GPS vertical velocities. All GPS velocities are relative to the stable Caribbean Plate [*Feng et al.*, 2012].

4. Modeling

4.1. Modeling Method

We used a back slip model to invert for the slip deficit on the plate interface [*Savage*, 1983], assuming that the interseismic strain accumulation is elastic. The back slip approximates the coupling on the plate interface. Regions where the back slip is the same as the plate motion rate are considered to be fully coupled [e.g., *Hetland and Simons*, 2010; *Liu et al.*, 2010a; *Savage*, 1983; *Wang and Dixon*, 2004].

The plate interface geometry is adopted from the model of *Feng et al.* [2012], which was derived from the slab seismicity [*Ghosh et al.*, 2008]. The plate dip angle changes from the surface to a depth of 62 km. From the trench to a depth of 18.6 km, the dip angle has a constant value of 11.4°. Below the depth of 18.6 km, a parabolic function is fit to the dip angle change, which has a maximum dip angle of 48.1° at a depth of 62 km (Figure 6b). The total interface has a length of 200 km along the trench strike direction and a width of 145 km along the dip direction. It is discretized into 40 × 29 rectangular patches with a patch size of 5 km × 5.1 km (Figure 6a).

Since oblique convergence has been suggested to be accommodated mostly by fore-arc sliver motion rather than strike-slip motion on the plate interface during the interseismic period [*Feng et al.*, 2012; *Norabuena et al.*, 2004], and the strike-slip motion is negligible relative to the dip-slip motion on the

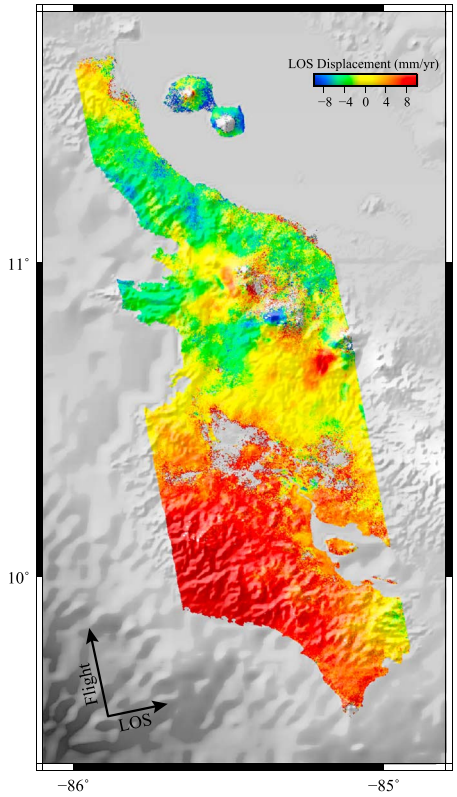

Figure 4. Linear deformation rate map derived from the linear regression of the deformation time series at each pixel. Positive displacements indicate surface motion away from the satellite.

plate interface (see the supporting information), we only consider the back slip component along the dip direction. We resolved the 3-D GPS velocities to trench-normal and vertical components, which provide good constraints on the downdip transition depth from locked to aseismic creeping. We excluded GPS stations near the volcanic arc due to possible contamination from volcanic deformation (Figure 6a). The linear inverse problem is

$$\begin{bmatrix} aW_{SAR}G_{SAR} & I \\ W_{GPS}G_{GPS} & 0 \\ \gamma D & 0 \end{bmatrix} \begin{bmatrix} U \\ C \end{bmatrix} = \begin{bmatrix} aW_{SAR}d_{SAR} \\ W_{GPS}d_{GPS} \\ 0 \end{bmatrix}$$

where U is a $M \times 1$ slip vector along the fault dip direction; M is the number of fault patches; C is the nuisance offset between GPS and InSAR; a is the relative weighting ratio between InSAR and GPS; W_{SAR} is a weighting matrix for the InSAR data set, which satisfies $W_{SAR}^T * W_{SAR} = \sum_{SAR}^{-1}, \sum_{SAR}$ is the InSAR data covariance matrix; G_{SAR} is the $N \times M$ Green function matrix with the elastic response at each InSAR pixel for unit dip slip at each fault patch; N is the number of InSAR pixels; I is a $N \times 1$ vector whose elements are all one; d_{SAR} is a $N \times 1$ displacement vector at each InSAR pixel; W_{GPS} is a weighting matrix for the GPS data set, which satisfies $W_{GPS}^T * W_{GPS} = \sum_{GPS}^{-1}, \sum_{GPS}$ is the GPS data covariance matrix; G_{GPS} is a $3N_2 \times M$ Green function matrix, which is the elastic response in the north, east, and vertical directions at each GPS station for unit dip slip at each fault patch; N_2 is the number of GPS stations; and d_{GPS} is a $3N_2 \times 1$ displacement vector including the east, north, and up components. $D = \nabla^2$ is a $M \times M$ Laplace smoothing matrix that is a scale-dependent second-order finite difference operator along both dip and strike directions, and γ is the smoothing factor. All the Green functions are calculated using an elastic dislocation model in a half space [*Okada*, 1985]. The covariance matrix of the GPS Σ_{GPS} is $diag\{\sigma_{1e}^2, \sigma_{1n}^2, \sigma_{1u}^2, \ldots, \sigma_{ie}^2, \sigma_{in}^2, \sigma_{iu}^2\}$, where $\sigma_{ie}^2, \sigma_{in}^2, \sigma_{iu}^2$ is the standard deviation of the east, north, and vertical components of the ith GPS. The GPS error estimation accounts for both the time-uncorrelated and time-correlated noise [*Feng et al.*, 2012]. The covariance matrix of InSAR is calculated based on the estimated covariance function in section 2.5.

We investigate the effect of the different weighting factors between InSAR and GPS on the inversion by varying this parameter from 0.1 to 10. The higher weighting of InSAR provides a better fit to the InSAR but a worse fit to the GPS data. We find a weight of 4.2:1 between InSAR and GPS which provides a good balance between fitting both the InSAR and GPS data (Figure 6c).

Our model is solved by using a least squares constrained inversion. The back slip rate at each fault element is constrained between zero and the trench-normal convergence rate between the Cocos and Caribbean plates (Co-CA). We impose a zero slip constraint at the trench and free slip at all other fault boundaries. Imposing zero slip constraints on all the fault boundaries does not change the inversion results. The smoothing factor γ is determined by the trade-off between model roughness and weighted data misfit (Figure 7d). Larger smoothing factors reduce the roughness of the model but increase data misfit [*Feng et al.*, 2012; *Jónsson et al.*, 2002; *Liu et al.*, 2010a]. The weighted root-mean-square (WRMS) residual is used for the model misfit. We choose $\lambda = 1$ as the preferred smoothing factor, which provides a balance between the roughness and WRMS residual (Figure 7d). This preferred model fits both the InSAR and GPS data well (Figure 8).

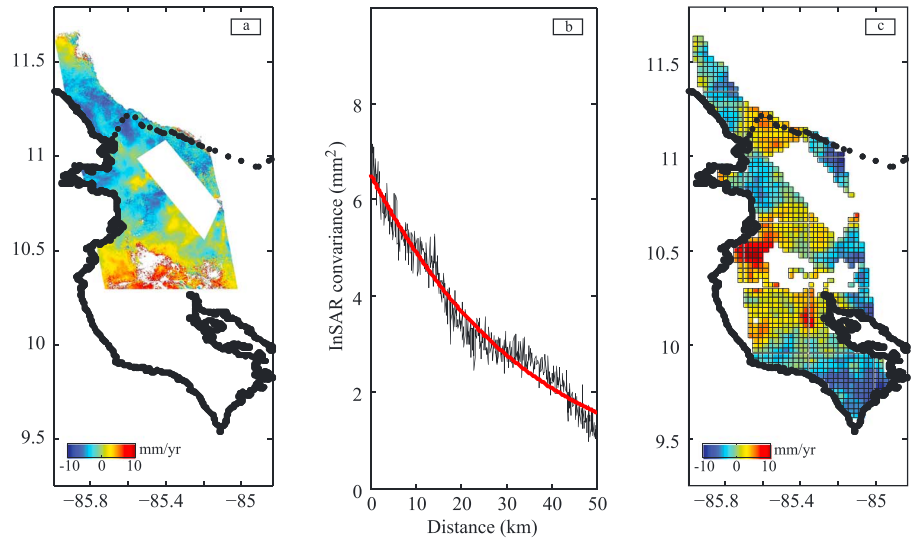

Figure 5. (a) The masked linear rate velocity map used for atmosphere noise estimation. (b) The 1-D covariance from the masked linear rate velocity map shown in Figure 5a. The black line is the estimated covariogram, and the red line is the best fit of covariance function. (c) Quadtree sampled synthetic atmospheric noise by using covariance function.

4.2. Checkerboard Resolution Test

To examine the spatial resolution in our model, we performed a checkerboard test. Since the average length scale of the coupling pattern in the resulting model is ~40 × 40 km^2, we divided the fault surface into patches of this size and imposed alternating full and zero back slip as the synthetic input model (Figure 9a). We then calculated the surface displacement at the GPS stations and the LOS displacement at each SAR pixel. We added random noise to the synthetic GPS velocities. The random noise follows a normal distribution with zero mean and the same uncertainty as the observed GPS data. We also added synthetic atmospheric noise (Figure 5c) to the synthetic InSAR data to assess the effect of spatially coherent noise on the inversion. The covariance matrices of GPS and InSAR used in the checkerboard tests are the same as used in the modeling. The same inversion method was applied to the checkerboard test, and the results using different smoothing factors are shown in Figures 9b–9d. All the tests show that the region under the Nicoya Peninsula is well resolved with little resolution near the trench and reduced resolution downdip on the fault interface. After testing the effect of different smoothing factors on the resolution, we find a factor of 1 which provides the best spatially recovered pattern.

4.3. Modeling Results

Our preferred model shows three robust strongly coupled regions (Figure 10). One patch locates beneath the middle portion of the Nicoya Peninsula centered at ~22 km depth. This locked region is very consistent for different smoothing factors (Figure 7) and coincides well with the rupture area of the 2012 M_w 7.6 Nicoya, Costa Rica, earthquake. The second locked patch locates just offshore the central Peninsula, centered at ~14 km depth and is nearly parallel to the first patch. This feature persists even when a larger smoothing factor is used. This region experienced little slip during the 2012 Nicoya, Costa Rica, earthquake. The third strongly locked patch locates offshore the southeastern end of the Nicoya Peninsula, and the coupling pattern close to the coastline is a robust feature and appears in results using different smoothing factors. This area also overlaps part of the rupture area of the 1990 M_w 7.0 Gulf of Nicoya earthquake (see Figure 11). The model indicates another strongly coupled region at the downdip edge of the fault; however, because it occurs in an area of low resolution due to a data gap and high noise near the inlet to the Nicoya Gulf, we do not believe that it is reliable. The accumulated geodetic strain moment rate of the first strongly coupled patch (an ~1100 km^2 area defined by the 70% locking contour) is equivalent to ~2.2 × 10^{18} Nm/yr (assuming a rigidity of 30 GPa). If this rate is assumed to be constant, the accumulated strain between 1950 and 2012 corresponds to a M_w 7.3 (~1.3 × 10^{20} Nm) earthquake. The accumulated moment rate of the central offshore locked patch is ~1.4 × 10^{18} Nm/yr (fault area of ~765 km^2), corresponding to a M_w 7.2 earthquake over this same 62 year period.

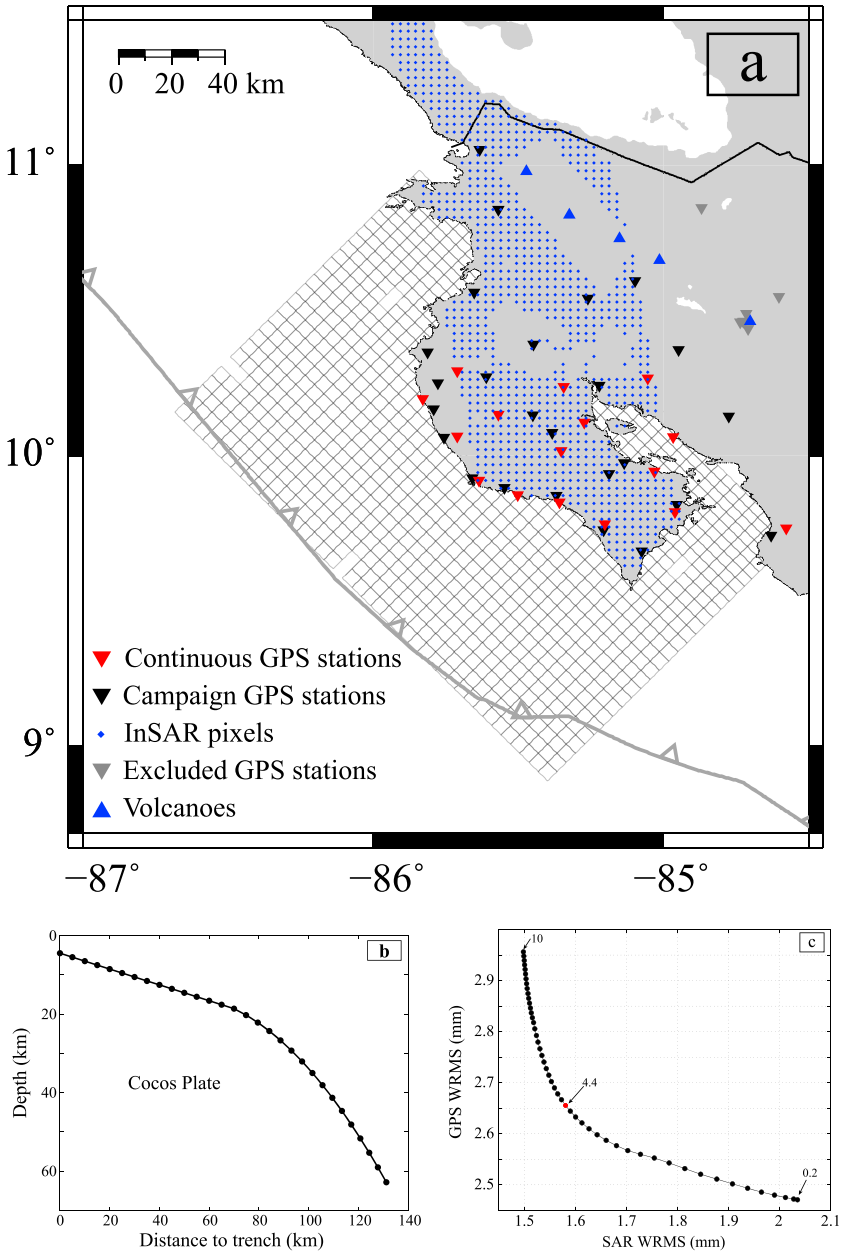

Figure 6. Fault model parameterization. (a) Surface projection of the fault plane model with grid spacing of 5 km along strike and dip direction, respectively. The red inverted triangles indicate the location of the continuous GPS stations, and the black inverted triangles indicate the location of the campaign GPS stations. The blue diamonds indicate the location of the InSAR pixels. The gray triangles indicate the location of the excluded GPS stations. The blue triangles are the Holocene active volcanoes [*Siebert and Simkin*, 2002]. (b) Cross section of the plate interface used in our model. The black nodes denote the ends of the planar row segments. (c) Trade-off curve between the weighted root mean square (WRMS) errors of both InSAR and the GPS. The preferred weight number is 4.2, which can fit both InSAR and GPS well.

Our model also indicates several regions with partial coupling (~55% locking; Figure 10): two patches downdip of the onshore strongly coupled region and one patch offshore of the northwestern part of the Nicoya Peninsula. The two downdip partially coupled regions are directly beneath land with excellent data coverage, so they are robustly resolved. The partially coupled area offshore to the northwest is also well resolved near the coastline, based on the resolution tests (Figure 9c).

The updip limit of our preferred coupling model is at ~10 km depth, which is shallower than the upper limit of microearthquakes in this region [*Newman et al.*, 2002], and the depth of the 100°C isotherm [*Harris et al.*, 2010]

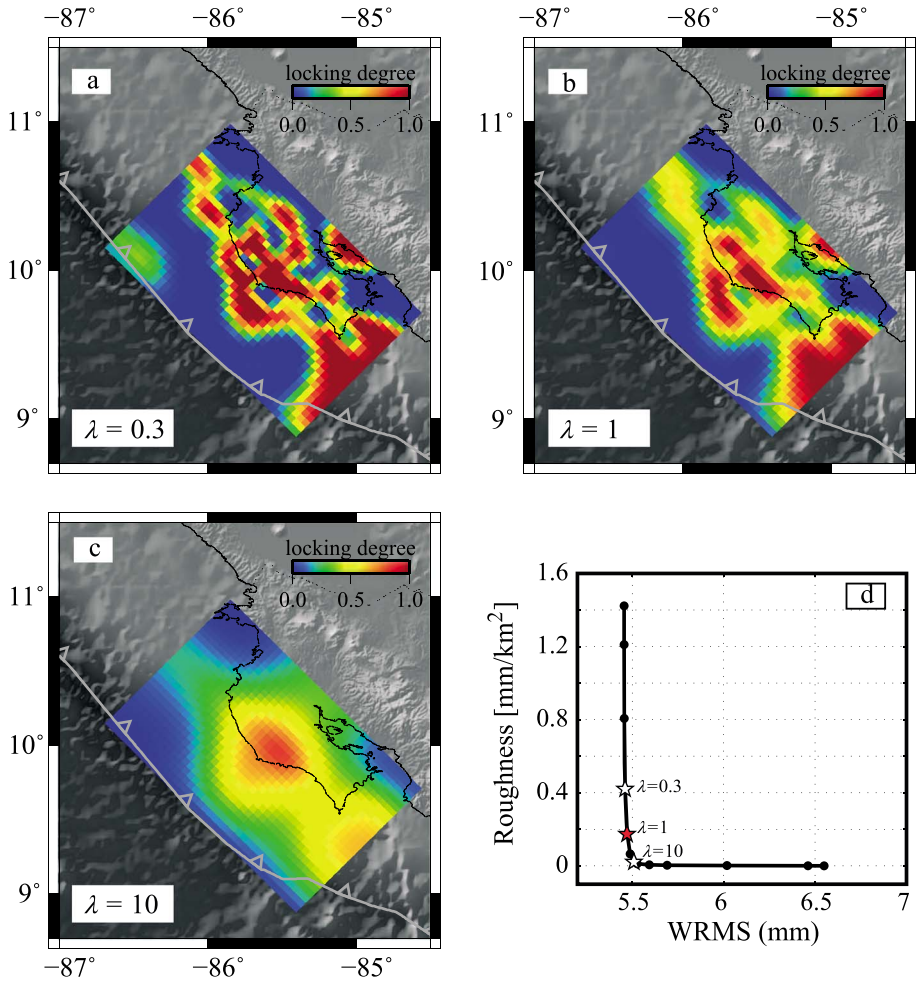

Figure 7. Surface projection of interseismic locking pattern for selected smoothing factors λ: (a) $\lambda = 0.3$, (b) $\lambda = 1$, (c) $\lambda = 10$. (d) Trade-off curve between model roughness and the weighted root mean square (WRMS) residual of the model fit. Our preferred smoothing factor $\lambda = 1$ provides a balance between the roughness and the model misfit. The data set includes both GPS and InSAR data, and a weighting factor between GPS and InSAR of 1:4.2 for all the models with different smoothing factors.

although admittedly this updip limit is not well constrained because of a lack of data offshore. The downdip limit of coupling does not appear as an abrupt transition (Figure 10). The depth of the deepest strong coupling (<70%) is ~24 km, while 55% coupling persists to almost 40 km depth.

5. Discussion

5.1. Interseismic Strain Accumulation

Slow slip, like earthquake motion occurs in the opposite direction of interseismic locking on the plate interface and releases part of the accumulated strain [e.g., *Liu et al.*, 2010b; *Beroza and Ide*, 2011]. The long-term accumulated elastic strain therefore includes the effect of any SSEs [e.g., *Correa-Mora et al.*, 2008; *Outerbridge et al.*, 2010]. Both GPS and InSAR data reflect the long-term strain accumulation averaged over several SSEs. The GPS data set we utilized is the velocity averaged over many years and includes transient offsets due to several SSEs [*Feng et al.*, 2012]. The InSAR linear rate map is also an average velocity over 4 years that includes the occurrences of several SSEs. Therefore, our resulting coupling model investigates the average interseismic strain accumulation rather than "inter-transient" strain accumulation.

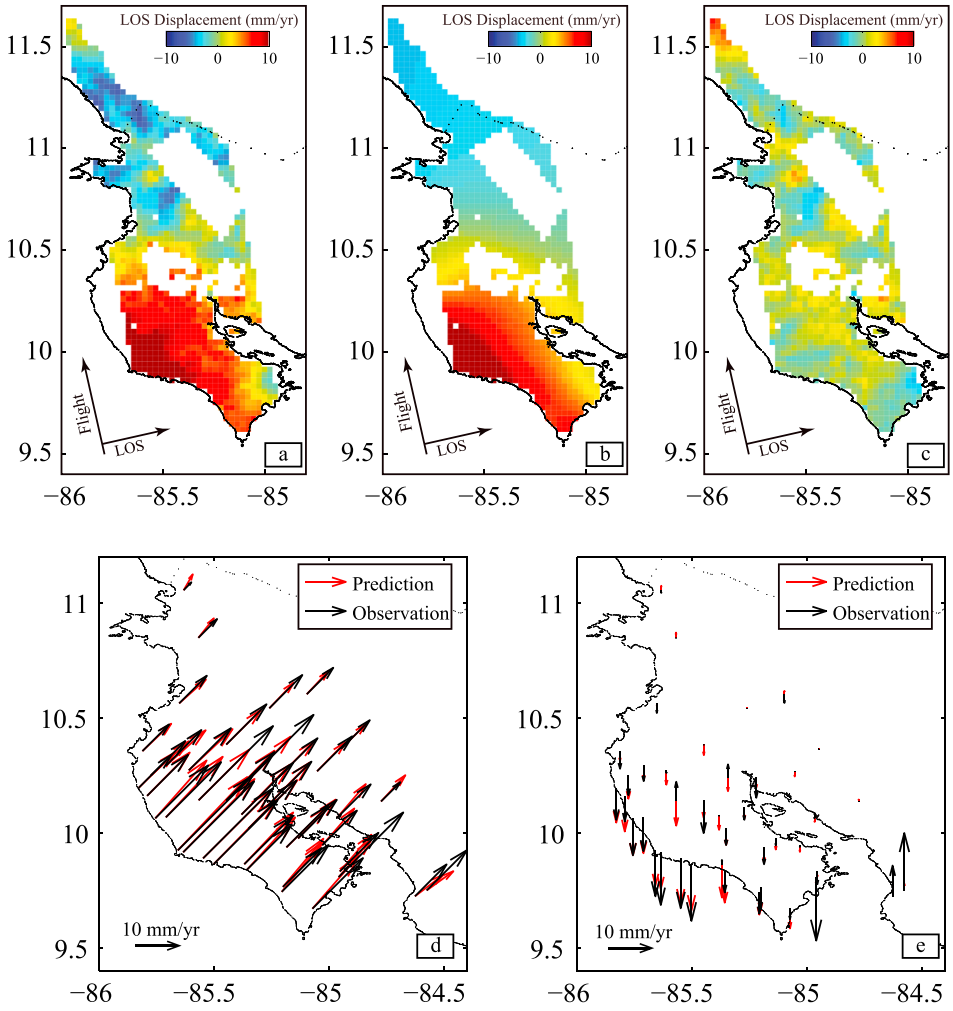

Figure 8. Misfit of the preferred back slip model to the observed data (a) Quadtree sampled InSAR linear rate velocity. (b) Predicted surface displacement in LOS direction from the preferred model. (c) LOS residual. (d) Predicted GPS horizontal velocity (red) versus the observed GPS horizontal velocity (black). (e) Predicted GPS vertical velocity (red) versus the observed GPS vertical velocity (black).

5.2. Comparison to the GPS-Only Coupling Model

Our preferred GPS/InSAR integrated model is similar to the GPS-only model in its long-wavelength features but differs from it in detail. Although both models contain two strongly coupled patches, one beneath and the other offshore the central part of the Peninsula, the two strongly coupled patches have slightly different spatial patterns in the two models (Figure 10). The onshore locked patch in the GPS-only model extends to greater depth and is indented or notched compared with the integrated model. The central offshore locked patch in the two models has a similar depth but clear variations along strike. The GPS-only model shows moderate coupling south of the boundary between Cocos-Nazca spreading center and East Pacific Rise derived crust, while the integrated model indicates strong coupling south of this boundary (Figure 10). The two strongly locked patches in the integrated model also have more separation along dip and more elongation along strike. The high resolution of these two strongly locked patches (Figure 9) and their robustness (see Text S6 in the supporting information) suggests these differences between the InSAR/GPS integrated and the GPS-only models are statistically significant. The third strongly locked region just offshore the southeastern portion of the Peninsula is more prominent in the integrated model than in the GPS-only model. This region is near the edge of our grid, and a portion has poor resolution (Figure 9), so we have less confidence in the difference between the models in this area.

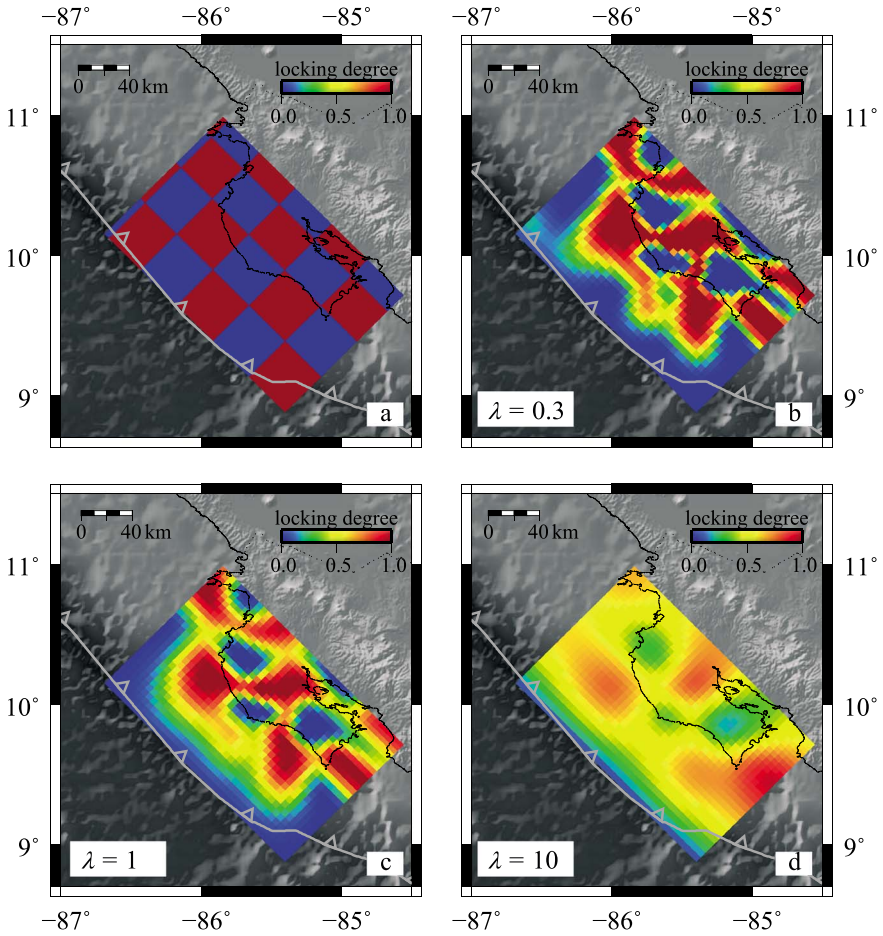

Figure 9. Checkerboard test showing the spatial resolution of the joint inversion of GPS and InSAR. (a) The imposed locking pattern, (b) recovered locking pattern at $\lambda = 0.3$ using the same inversion method and data distribution as in the real data set, (c) recovered locking pattern at $\lambda = 1$ which is our preferred smooth factor, and (d) recovered locking pattern at $\lambda = 10$. The weighting factor between GPS and InSAR is 1:4.2.

In contrast to these somewhat subtle differences in the strongly coupled regions, the two models are significantly different in the distribution of partially coupled regions and the transition from strong to weak coupling. For example, our integrated model reveals two onshore partially coupled areas with ~55% locking downdip of the strongly locked patch (Figure 10), while the GPS-derived model reveals very low coupling (0–30% coupling) in these two areas [*Feng et al.*, 2012]. This difference between models beneath the land reflects a better resolution of the combined InSAR and GPS data set (see Text S7 in the supporting information). Moreover, an elongated ~55% locked patch exists in the northwestern offshore region in the integrated model, while this partially coupled feature appears stronger and extends further inland in the GPS-only model. Similarly, a downdip ~55% coupled region in the GPS-only model appears to be uncoupled in our integrated model (northwestern most part of the peninsula in Figure 10). Another downdip ~55% coupled region to the southeast is not well resolved in either model. The integrated model images an abrupt updip transition from strong to zero coupling about halfway between the shoreline and the trench while the GPS-derived model shows a much smoother transition. In general, we find that the integrated and GPS-only models share similar long-wavelength characteristics, but inclusion of InSAR data improves model resolution and reveals more refined features at the local scale.

5.3. Comparison With Local Seismic and Aseismic Events

The 5 September 2012 M_w 7.6 Nicoya earthquake nucleated offshore and ruptured down dip with the largest slip occurring coincident with the onshore strongly coupled patch as anticipated [*Protti et al.*, 2014; *Yue et al.*, 2013], while most of the central offshore strongly coupled patch remained intact. The 2012 coseismic rupture

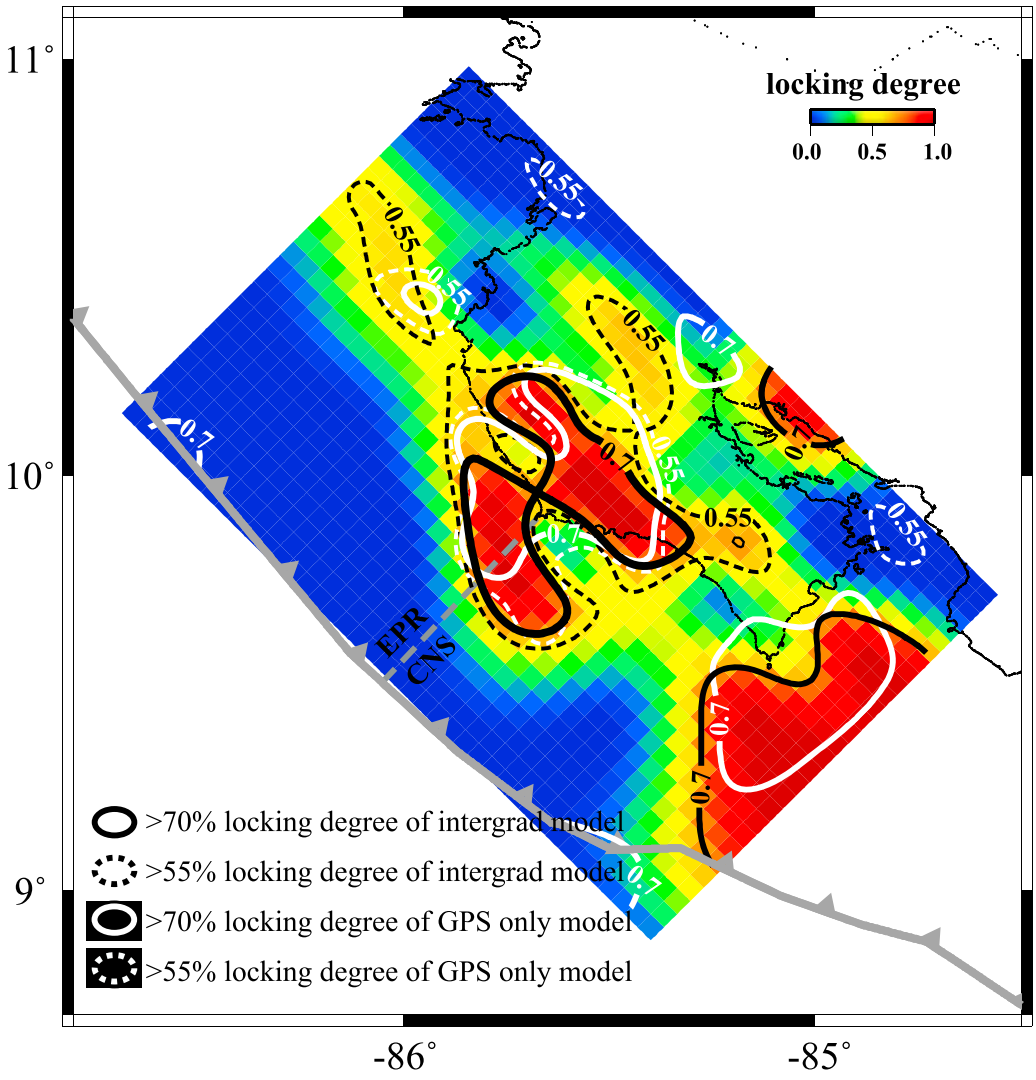

Figure 10. Comparison between the integrated interseismic coupling model and the GPS-only model. The regions of our model with coupling degree >70% are outlined by the solid black lines, and the regions with coupling degree >55% are outlined by the dashed black lines. The regions of *Feng et al.* [2012] with coupling degree >70% are outlined by the solid white lines, and the regions with coupling degree >55% are outlined by the white dashed lines.

extended into the transition region from strong to weak coupling (Figure 11), which suggests that dynamic rupture is capable of penetrating into regions with conditional stability. Most thrust aftershocks of the 2012 event occurred near the upper edge of the onshore strongly coupled patch that failed in the earthquake (Figure 11). Few of these aftershocks and any previously identified plate boundary events [*DeShon et al.*, 2006] locate in the central offshore strongly coupled patch. The lack of coseismic and interseismic slip on this patch suggests a different mechanical behavior from the onshore locked patch. The fate of the central offshore locked patch and its mode of future failure are unclear. It may have the potential to generate a future large earthquake (M_w 7.2 as estimated in section 4.3). However, the occurrence of afterslip (R. Malservisi, personal communication, 2014), its proximity to geodetically determined slow slip [*Dixon et al.*, 2014] and accompanying tremor, and very low frequency earthquakes (see supporting information) suggest that this region may have released some of the accumulated strain. A recent inversion of the GPS data using a refined 3-D plate interface model for the Nicoya Peninsula produced a muted offshore locking pattern [*Kyriakopoulos et al.*, 2013]. The significantly reduced offshore strain accumulation of their model may in part be released during aseismic transient events. The third strongly locked region offshore the southeast

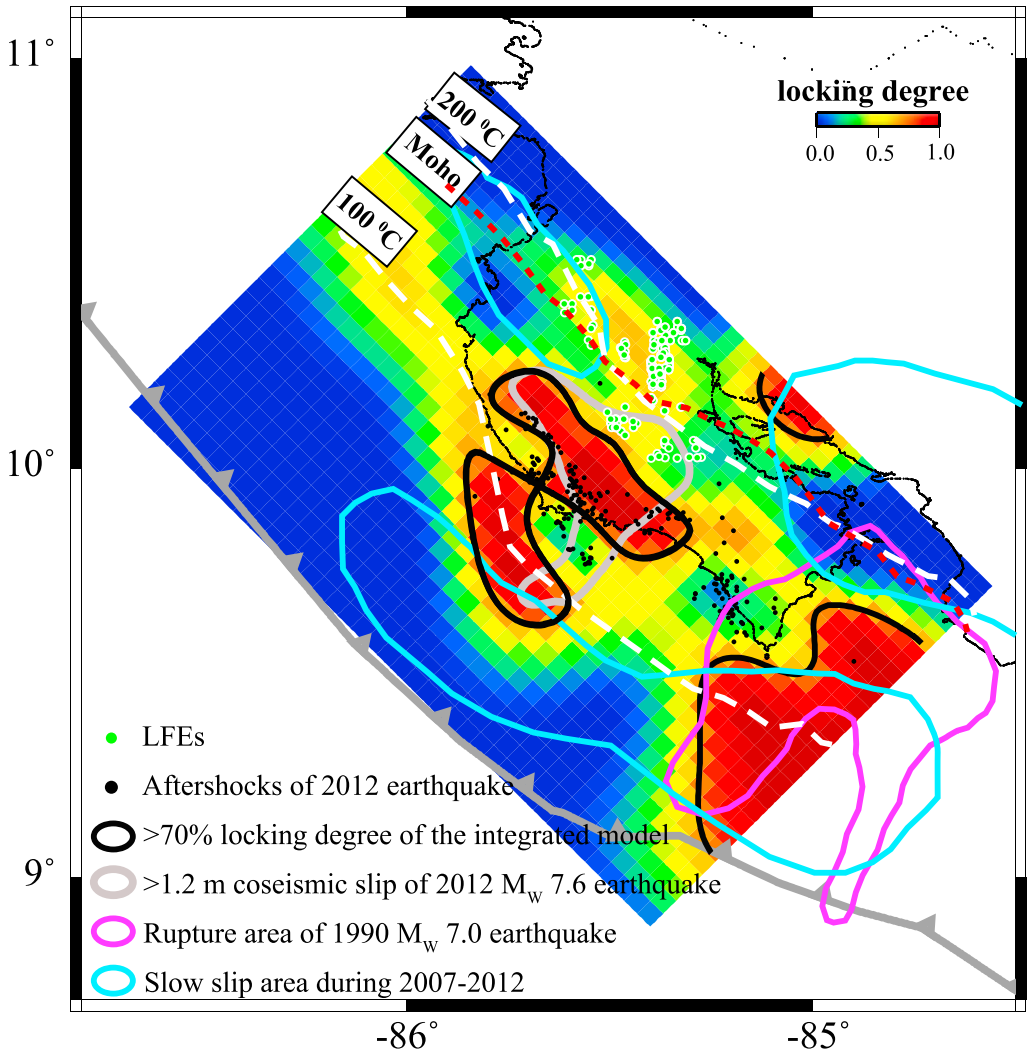

Figure 11. Comparison between the integrated interseismic coupling model and local seismic and aseismic events. The regions of our model with coupling degree >70% are outlined in solid black lines. The region of coseismic slip >1.2 m is outlined in gray color. The coseismic rupture zone of 1990 M_w 7.0 earthquake is outlined in pink color. The sum of the slow slip during 2007–2012 is outlined in the light blue color [*Dixon et al.*, 2014]. Low-frequency earthquakes (LFE) [*Brown et al.*, 2009] are plotted with green-filled, white-bordered circles. Thrust aftershocks of the 2012 event are indicated with black dots. The 110°C and 200°C isotherms are indicated as the white dashed lines [*Harris et al.*, 2010], and the Moho is indicated as the red dashed line.

part of the Peninsula that overlaps the rupture area of the 1990 M_w 7.0 earthquake did not slip during the 2012 Nicoya earthquake, and we believe that it has the potential to fail in another future earthquake.

Large slow-slip events (SSEs) have occurred repeatedly on the plate interface near Nicoya every 21 ± 6 months, while smaller events are much more frequent [*Jiang et al.*, 2012; *Dixon et al.*, 2014]. All of the SSEs are accompanied by tremor with both low-frequency (LFE) and very low frequency earthquakes embedded within this tremor [*Brown et al.*, 2009; *Walter et al.*, 2013]. There were seven SSEs recorded by GPS stations between 2007–2012, and all had some slip both updip and downdip of the seismogenic zone [*Outerbridge et al.*, 2010; *Dixon et al.*, 2014]. A comparison of slow slip locations with the coupling pattern of our model shows that downdip slow slip mainly occurs in the weakly coupled regions (locking <55%), while updip slow slip overlaps part of the strongly locked areas (Figure 11). A more detailed interpretation of the relative locations of these features should consider the different fault geometries used in the inversion schemes.

The abundant tremor and very low frequency earthquakes that accompany slow slip are poorly located but corroborate the overlap of slow-slip phenomena with the offshore locked patch (supporting information). If shallow slow slip indeed overlaps part of the strongly coupled region, it suggests that strain accumulation may be in part released by the recurrent SSEs in the shallow seismogenic zone in Costa Rica, similar to what has been found in other subduction zones [e.g., *Liu et al.*, 2010b; *Beroza and Ide*, 2011]. The overlap of stick-slip and slow-slip behavior may be real or more likely reflects our inability to distinguish small length-scale variations in frictional behavior due to limited resolution. Closely located brittle and viscous deformation modes have been shown to exist in rock assemblages from exhumed subduction zones [*Fagereng and Sibson*, 2010]. These authors proposed that subduction plate boundary shear zones are very heterogeneous and may consist of alternating weak and strong components that can host seismic and aseismic deformation modes within a small volume.

Brown et al. [2009] located deep low-frequency earthquakes (LFEs) in Costa Rica using a network autocorrelation approach, which allows individual *S* waves to be identified. These LFEs are the most accurately located slow-slip phenomena in the region and occur over a depth range of 30–40 km on the plate interface. They mainly occur in the partially locked (~55%) areas at the transition from strong to weak coupling just downdip of the strongly locked patch (Figure 11). LFEs and partial coupling indicate the transition in frictional properties from stick slip to stable sliding.

Integration of our coupling model with the local seismic/aseismic events provides some insights into possible mechanisms producing variations in locking behavior of the Nicoya, Costa Rica, subduction interface. The fact that the 100°C isotherm intersects the central offshore strongly coupled region, and the 200°C isotherm occurs deeper than the dowdip limit of locking, suggests that temperature is not the primary control on coupling variations in Nicoya, Costa Rica. Similar conclusions were also drawn for the Hikirangi subduction zone, New Zealand, and the Cascadia subduction zone [*McCaffrey et al.*, 2008; *Gomberg*, 2010]. Numerical models show that SSEs typically occur at transitions from velocity weakening to velocity strengthening [e.g., *Liu and Rice*, 2005; *Liu and Rice*, 2007]. The coincidence of SSEs with low coupling in our model suggests that differences in frictional properties are an important factor affecting coupling variations. The occurrence of LFEs, and slow slip, in general, has been attributed to fluid-rich environments with high pore pressure [*Schwartz and Rokosky*, 2007; *Shelly*, 2010]. Previous studies in Costa Rica indicate that the fluid production is very high at both shallow and deep depths along the subducting plate interface beneath Nicoya Peninsula [e.g., *Tryon et al.*, 2010; *Hensen et al.*, 2004; *Audet and Schwartz*, 2013]. Dehydration of clay minerals in the subducted marine sediments at shallow depth and serpentinization at deep depth could provide sources for such high fluid production [*Tryon et al.*, 2010; *Hensen et al.*, 2004; *DeShon and Schwartz*, 2004]. In this regard, fluid distribution at the plate interface may be another important factor contributing to the observed coupling variations in the Costa Rica subduction zone.

6. Conclusions

The interseismic InSAR linear rate map for the Nicoya Peninsula reveals a LOS deformation rate on the southern coastline of ~10–15 mm/yr that gradually decreases inland from the trench. Our study demonstrates that InSAR data can be used to recover small, long-wavelength deformation signals in challenging subduction zone environments when integrated with GPS observations. The interseismic coupling model using both GPS and InSAR data reveals three robust strongly coupled regions: (1) beneath the middle portion of the Nicoya Peninsula centered at ~22 km depth; (2) offshore the central part of the peninsula, parallel to the first patch; and (3) offshore the southeast end of the peninsula. The first patch ruptured during the 2012 M_w 7.6 Costa Rica earthquake as expected. The second patch did not, and its mode of future failure is unclear. It might have the potential for a future seismic event of ~M_w 7.2, or much of its accumulated strain may be released by slow slip. The third strongly coupled patch overlaps part of the rupture area of the Gulf of Nicoya 1990 M_w 7.0 earthquake and will likely slip again in a future earthquake.

Our integrated model and the GPS-only model share similar long-wavelength characteristics, but inclusion of InSAR data improves model resolution and reveals more refined features at local scales. This allows for improved comparison with local seismic and aseismic events. Well-located low-frequency earthquakes that accompany slow slip occur at downdip transitions from strong to weak coupling. Geodetically detected

deep slow slip tends to occur in weakly coupled regions, while updip slow slip may overlap with strongly locked areas and help to release part of the accumulated strain. The spatial correlation between the distribution of coupling and the locations of SSEs and LFEs suggests that fluid and frictional heterogeneities may be the two main factors influencing coupling variations.

Acknowledgments

This study was supported by OCE-0841061 and EAR-1321550. ALOS PALSAR data are copyright JAXA/METI and were provided by the GEO Supersites and the U.S. Government Research Consortium Data pool at the Alaska Satellite Facility (https://www.asf.alaska.edu/). The research described in this paper was carried out in part at the Jet Propulsion Laboratory, California Institute of Technology, under a contract with the National Aeronautics and Space Administration. We greatly appreciate the support of Emily Brodsky, and thank all the people who provided advice on this project. Figures were created using Generic Mapping Tools [*Wessel and Smith*, 1991]. We thank M.E. Prichard and an anonymous reviewer for their very helpful comments that greatly improved this paper as well Scott Baker, Tim Dixon, Rowena Lohman and Isabelle Ryder for their early guidance on this project.

References

Audet, P., and S. Y. Schwartz (2013), Hydrologic control of forearc strength and seismicity in the Costa Rican subduction zone, *Nat. Geosci.*, *6*(10), 852–855.

Bejar-Pizarro, M., A. Socquet, R. Armijo, D. Carrizo, J. Genrich, and M. Simons (2013), Andean structural control on interseismic coupling in the North Chile subduction zone, *Nat. Geosci.*, *6*(6), 462–467.

Berardino, P., G. Fornaro, R. Lanari, and E. Sansosti (2002), A new algorithm for surface deformation monitoring based on small baseline differential SAR interferograms, *IEEE Trans. Geosci. Remote Sens.*, *40*(11), 2375–2383.

Beroza, G. C., and S. Ide (2011), Slow earthquakes and nonvolcanic tremor, *Annu. Rev. Earth Planet. Sci.*, *39*, 271–296.

Biggs, J., T. Wright, Z. Lu, and B. Parsons (2007), Multi-interferogram method for measuring interseismic deformation: Denali fault, Alaska, *Geophys. J. Int.*, *170*(3), 1165–1179.

Biggs, J., D. P. Robinson, and T. H. Dixon (2009), The 2007 Pisco, Peru, earthquake (M8.0): Seismology and geodesy, *Geophys. J. Int.*, *176*(3), 657–669.

Brown, J. R., G. C. Beroza, S. Ide, K. Ohta, D. R. Shelly, S. Y. Schwartz, W. Rabbel, M. Thorwart, and H. Kao (2009), Deep low-frequency earthquakes in tremor localize to the plate interface in multiple subduction zones, *Geophys. Res. Lett.*, *36*, L19306, doi:10.1029/2009GL040027.

Bürgmann, R., P. A. Rosen, and E. J. Fielding (2000), Synthetic aperture radar interferometry to measure Earth's surface topography and its deformation, *Annu. Rev. Earth Planet. Sci.*, *28*(1), 169–209.

Cavalié, O., C. Lasserre, M. P. Doin, G. Peltzer, J. Sun, X. Xu, and Z. K. Shen (2008), Measurement of interseismic strain across the Haiyuan fault (Gansu, China), by InSAR, *Earth Planet. Sci. Lett.*, *275*(3–4), 246–257.

Cavalié, O., E. Pathier, M. Radiguet, M. Vergnolle, N. Cotte, A. Walpersdorf, V. Kostoglodov, and F. Cotton (2013), Slow slip event in the Mexican subduction zone: Evidence of shallower slip in the Guerrero seismic gap for the 2006 event revealed by the joint inversion of InSAR and GPS data, *Earth Planet. Sci. Lett.*, *367*, 52–60.

Chen, C. W., and H. A. Zebker (2000), Network approaches to two-dimensional phase unwrapping: Intractability and two new algorithms, *JOSA A*, *17*(3), 401–414.

Correa-Mora, F., C. DeMets, E. Cabral-Cano, B. Marquez-Azua, and O. Diaz-Molina (2008), Interplate coupling and transient slip along the subduction interface beneath Oaxaca, Mexico, *Geophys. J. Int.*, *175*(1), 269–290.

DeMets, C., R. G. Gordon, and D. F. Argus (2010), Geologically current plate motions, *Geophys. J. Int.*, *181*(1), 1–80.

DeShon, H. R., and S. Y. Schwartz (2004), Evidence for serpentinization of the forearc mantle wedge along the Nicoya Peninsula, Costa Rica, *Geophys. Res. Lett.*, *31*, L21611, doi:10.1029/2004GL021179.

DeShon, H. R., S. Y. Schwartz, A. V. Newman, V. González, M. Protti, L. M. Dorman, T. H. Dixon, D. E. Sampson, and E. R. Flueh (2006), Seismogenic zone structure beneath the Nicoya Peninsula, Costa Rica, from three-dimensional local earthquake P- and S-wave tomography, *Geophys. J. Int.*, *164*(1), 109–124.

Dixon, T. H. (1993), GPS measurement of relative motion of the Cocos and Caribbean Plates and strain accumulation across the Middle America Trench, *Geophys. Res. Lett.*, *20*(20), 2167–2170, doi:10.1029/93GL02415.

Dixon, T. H., Y. Jiang, R. Malservisi, R. McCaffrey, N. Voss, M. Protti, and V. Gonzalez (2014), Earthquake and tsunami forecasts: Relation of slow slip events to subsequent earthquake rupture, *Proc. Natl. Acad. Sci. U.S.A.*, *111*(48), 17,039–17,044.

Fagereng, Å., and R. H. Sibson (2010), Melange rheology and seismic style, *Geology*, *38*(8), 751–754.

Fattahi, H., and F. Amelung (2014), InSAR uncertainty due to orbital errors, *Geophys. J. Int.*, *199*(1), 549–560.

Feng, L., A. V. Newman, M. Protti, V. González, Y. Jiang, and T. H. Dixon (2012), Active deformation near the Nicoya Peninsula, northwestern Costa Rica, between 1996 and 2010: Interseismic megathrust coupling, *J. Geophys. Res.*, *117*(B6), B06407, doi:10.1029/2012JB009230.

Fialko, Y. (2006), Interseismic strain accumulation and the earthquake potential on the southern San Andreas fault system, *Nature*, *441*(7096), 968–971.

Ghosh, A., A. V. Newman, A. M. Thomas, and G. T. Farmer (2008), Interface locking along the subduction megathrust from b-value mapping near Nicoya Peninsula, Costa Rica, *Geophys. Res. Lett.*, *35*, L01301, doi:10.1029/2007GL031617.

Gomberg, J. (2010), Slow-slip phenomena in Cascadia from 2007 and beyond: A review, *Geol. Soc. Am. Bull.*, *122*(7–8), 963–978.

Gourmelen, N., F. Amelung, and R. Lanari (2010), Interferometric synthetic aperture radar–GPS integration: Interseismic strain accumulation across the Hunter Mountain fault in the eastern California shear zone, *J. Geophys. Res.*, *115*, doi:10.1029/2009JB007064.

Hanssen, R. F. (2001), *Radar Interferometry: Data Interpretation and Error Analysis*, Kluwer Acad., Dordrecht, Netherlands.

Harris, R. N., G. Spinelli, C. R. Ranero, I. Grevemeyer, H. Villinger, and U. Barckhausen (2010), Thermal regime of the Costa Rican convergent margin: 2. Thermal models of the shallow Middle America subduction zone offshore Costa Rica, *Geochem. Geophys. Geosyst.*, *11*, Q12S29, doi:10.1029/2010GC003273.

Hensen, C., K. Wallmann, M. Schmidt, C. R. Ranero, and E. Suess (2004), Fluid expulsion related to mud extrusion off Costa Rica—a window to the subducting slab, *Geology*, *32*(3), 201–204.

Hetland, E. A., and M. Simons (2010), Post-seismic and interseismic fault creep II: Transient creep and interseismic stress shadows on megathrusts, *Geophys. J. Int.*, *181*(1), 99–112.

Hooper, A., D. Bekaert, K. Spaans, and M. Arıkan (2012), Recent advances in SAR interferometry time series analysis for measuring crustal deformation, *Tectonophysics*, *514–517*, 1–13.

Hyndman, R., K. Wang, and M. Yamano (1995), Thermal constraints on the seismogenic portion of the southwestern Japan subduction thrust, *J. Geophys. Res.*, *100*(B8), 15,373–15,392, doi:10.1029/95JB00153.

Jiang, Y., S. Wdowinski, T. H. Dixon, M. Hackl, M. Protti, and V. Gonzalez (2012), Slow slip events in Costa Rica detected by continuous GPS observations, 2002–2011, *Geochem. Geophys. Geosyst.*, *13*, Q04006, doi:10.1029/2012GC004058.

Jónsson, S., H. Zebker, P. Segall, and F. Amelung (2002), Fault slip distribution of the 1999 Mw 7.1 Hector Mine, California, earthquake, estimated from satellite radar and GPS measurements, *Bull. Seismol. Soc. Am.*, *92*(4), 1377–1389.

Kyriakopoulos, C. A. V., R. Newman, T. H. Malservisi, J. I. Dixon, M. Walter, and V. G. Protti (2013), Geodetic and structural constraints on locking and failure around the 5 September 2012 Nicoya (Mw7.6), Costa Rica earthquake, Abstract presented at the Fall AGU meeting, G31C-04.

Liu, Y., and J. R. Rice (2005), Aseismic slip transients emerge spontaneously in three-dimensional rate and state modeling of subduction earthquake sequences, *J. Geophys. Res.*, *110*(B8), B08307, doi:10.1029/2004JB003424.
Liu, Y., and J. R. Rice (2007), Spontaneous and triggered aseismic deformation transients in a subduction fault model, *J. Geophys. Res.*, *112*(B9), B09404, doi:10.1029/2007JB004930.
Liu, Z., S. Owen, D. Dong, P. Lundgren, F. Webb, E. Hetland, and M. Simons (2010a), Estimation of interplate coupling in the Nankai trough, Japan using GPS data from 1996 to 2006, *Geophys. J. Int.*, *181*(3), 1313–1328.
Liu, Z., S. Owen, D. Dong, P. Lundgren, F. Webb, E. Hetland, and M. Simons (2010b), Integration of transient strain events with models of plate coupling and areas of great earthquakes in southwest Japan, 181, 1292–1312, *Geophys. J. Int.*, doi:10.1111/j.1365-246X.2010.04599.x.
Liu, Z., D. Dong, and P. Lundgren (2011), Constraints on time-dependent volcanic source models at Long Valley Caldera from 1996 to 2009 using InSAR and geodetic measurements, *Geophys. J. Int.*, *187*(3), 1283–1300.
Liu, Z., H. S. Jung, and Z. Lu (2014), Joint correction of ionosphere noise and orbital error in L-band SAR interferometry of interseismic deformation in southern California, *IEEE Trans. Geosci. Remote Sens.*, *52*(6), 3421–3427, doi:10.1109/TGRS.2013.2272791.
Lohman, R. B., and M. Simons (2005), Some thoughts on the use of InSAR data to constrain models of surface deformation: Noise structure and data downsampling, *Geochem. Geophys. Geosyst.*, *6*, doi:10.1029/2004GC000841.
López-Quiroz, P., M.-P. Doin, F. Tupin, P. Briole, and J.-M. Nicolas (2009), Time series analysis of Mexico City subsidence constrained by radar interferometry, *J. Appl. Geophys.*, *69*(1), 1–15.
Loveless, J. P., and B. J. Meade (2011), Spatial correlation of interseismic coupling and coseismic rupture extent of the 2011 MW= 9.0 Tohoku-oki earthquake, *Geophys. J. Int.*, *38*(17), L17306.
Mazzotti, S., X. Le Pichon, P. Henry, and S.-I. Miyazaki (2000), Full interseismic locking of the Nankai and Japan-west Kurile subduction zones: An analysis of uniform elastic strain accumulation in Japan constrained by permanent GPS, *J. Geophys. Res.*, *105*(B6), 13,159–13,177, doi:10.1029/2000JB900060.
McCaffrey, R., L. M. Wallace, and J. Beavan (2008), Slow slip and frictional transition at low temperature at the Hikurangi subduction zone, *Nat. Geosci.*, *1*(5), 316–320.
Metois, M., A. Socquet, and C. Vigny (2012), Interseismic coupling, segmentation and mechanical behavior of the central Chile subduction zone, *J. Geophys. Res.*, *117*(B3), B03406, doi:10.1029/2011JB008736.
Newman, A. V., S. Y. Schwartz, V. Gonzalez, H. R. DeShon, J. M. Protti, and L. M. Dorman (2002), Along-strike variability in the seismogenic zone below Nicoya Peninsula, Costa Rica, *Geophys. Res. Lett.*, *29*(20), 1977, doi:10.1029/2002GL015409.
Norabuena, E., T. H. Dixon, S. Schwartz, H. DeShon, A. Newman, M. Protti, V. Gonzalez, L. R. Dorman, E. R. Flueh, and P. Lundgren (2004), Geodetic and seismic constraints on some seismogenic zone processes in Costa Rica, *J. Geophys. Res.*, *109*, B11403, doi:10.1029/2003JB002931.
Okada, Y. (1985), Surface deformation due to shear and tensile faults in a half-space, *Bull. Seismol. Soc. Am.*, *75*(4), 1135–1154.
Outerbridge, K., T. Dixon, S. Schwartz, J. Walter, M. Protti, V. Gonzalez, J. Biggs, M. Thorwart, and W. Rabbel (2010), A tremor and slip event on the Cocos-Caribbean subduction zone as measured by a global positioning system (GPS) and seismic network on the Nicoya Peninsula, Costa Rica, *J. Geophys. Res.*, *115*(B10), B10408, doi:10.1029/2009JB006845.
Parsons, B., T. Wright, P. Rowe, J. Andrews, J. Jackson, R. Walker, M. Khatib, M. Talebian, E. Bergman, and E. Engdahl (2006), The 1994 Sefidabeh (eastern Iran) earthquakes revisited: New evidence from satellite radar interferometry and carbonate dating about the growth of an active fold above a blind thrust fault, *Geophys. J. Int.*, *164*(1), 202–217.
Pritchard, M. E., and E. J. Fielding (2008), A study of the 2006 and 2007 earthquake sequence of Pisco, Peru, with InSAR and teleseismic data, *Geophys. Res. Lett.*, *35*, L09308, doi:10.1029/2008GL033374.
Pritchard, M. E., M. Simons, P. A. Rosen, S. Hensley, and F. H. Webb (2002), Co-seismic slip from the 1995 July 30 Mw= 8.1 Antofagasta, Chile, earthquake as constrained by InSAR and GPS observations, *Geophys. J. Int.*, *150*(2), 362–376.
Protti, M., V. Gonzalez, A. V. Newman, T. H. Dixon, S. Y. Schwartz, J. S. Marshall, L. Feng, J. I. Walter, R. Malservisi, and S. E. Owen (2014), Nicoya earthquake rupture anticipated by geodetic measurement of the locked plate interface, *Nat. Geosci.*, *7*(2), 117–121.
Rosen, P. A., S. Henley, G. Peltzer, and M. Simons (2004), Updated repeat orbit interferometry package released, *Eos Trans. AGU*, *85*(5), 47–47.
Savage, J. (1983), A dislocation model of strain accumulation and release at a subduction zone, *J. Geophys. Res.*, *88*(B6), 4984–4996, doi:10.1029/JB088iB06p04984.
Schwartz, S. Y., and J. M. Rokosky (2007), Slow slip events and seismic tremor at circum-Pacific subduction zones, *Rev. Geophys.*, *45*, doi:10.1029/2006RG000208.
Shelly, D. R. (2010), Migrating tremors illuminate complex deformation beneath the seismogenic San Andreas fault, *Nature*, *463*(7281), 648–652.
Siebert, L., and T. Simkin (2002), *Volcanoes of the World: An Illustrated Catalog of Holocene Volcanoes and Their Eruptions*, Global Volcanism Program Digital Inf. Ser, vol. GVP-3, Smithsonian Inst., Washington, D. C. [Available at http://www.volcano.si.edu.]
Simons, M., and P. Rosen (2007), Interferometric synthetic aperture radar geodesy, in *Treatise on Geophysics - Geodesy*, vol. 3, edited by G. Schubert, pp. 391–446, Elsevier, Amsterdam.
Sudhaus, H., and J. Sigurjón (2009), Improved source modelling through combined use of InSAR and GPS under consideration of correlated data errors: Application to the June 2000 Kleifarvatn earthquake, Iceland, *Geophys. J. Int.*, *176*(2), 389–404.
Tong, X., D. Sandwell, K. Luttrell, B. Brooks, M. Bevis, M. Shimada, J. Foster, R. Smalley, H. Parra, and J. C. Báez Soto (2010), The 2010 Maule, Chile earthquake: Downdip rupture limit revealed by space geodesy, *Geophys. Res. Lett.*, *37*, doi:10.1029/2010GL045805.
Tong, X., D. Sandwell, and B. Smith-Konter (2013), High-resolution interseismic velocity data along the San Andreas Fault from GPS and InSAR, *J. Geophys. Res. Solid Earth*, *118*, 369–389, doi:10.1029/2012JB009442.
Tryon, M. D., C. G. Wheat, and D. R. Hilton (2010), Fluid sources and pathways of the Costa Rica erosional convergent margin, *Geochem. Geophys. Geosyst.*, *11*, doi:10.1029/2009GC002818.
Walter, J. I., S. Y. Schwartz, J. M. Protti, and V. Gonzalez (2011), Persistent tremor within the northern Costa Rica seismogenic zone, *Geophys. Res. Lett.*, *38*, doi:10.1029/2010GL045586.
Walter, J. I., S. Y. Schwartz, M. Protti, and V. Gonzalez (2013), The synchronous occurrence of shallow tremor and very low frequency earthquakes offshore of the Nicoya Peninsula, Costa Rica, *Geophys. Res. Lett.*, *40*, 1517–1522, doi:10.1002/grl.50213.
Wang, K., and T. Dixon (2004), "Coupling" Semantics and science in earthquake research, *Eos Trans. AGU*, *85*(18), 180–180.
Wessel, P., and W. H. F. Smith (1991), Free software helps map and display data, *Eos Trans. AGU*, *72*, 441, doi:10.1029/90EO00319.
Yue, H., T. Lay, S. Y. Schwartz, L. Rivera, M. Protti, T. H. Dixon, S. Owen, and A. V. Newman (2013), The 5 September 2012 Nicoya, Costa Rica Mw 7.6 earthquake rupture process from joint inversion of high-rate GPS, strong-motion, and teleseismic P wave data and its relationship to adjacent plate boundary interface properties, *J. Geophys. Res. Solid Earth*, *118*, 5453–5466, doi:10.1002/jgrb.50379.
Zweck, C., J. T. Freymueller, and S. C. Cohen (2002), Three-dimensional elastic dislocation modeling of the postseismic response to the 1964 Alaska earthquake, *J. Geophys. Res.*, *107*(B4), ECV 1-1–ECV 1–11, doi:10.1029/2001JB000409.